Influence of thickness and morphology of MoS_2 on the performance of counter electrodes in dye-sensitized solar cells

Lam Thuy Thi Mai[1], Hai Viet Le[*2,3], Ngan Kim Thi Nguyen[2,3], Van La Tran Pham[2,3], Thu Anh Thi Nguyen[1], Nguyen Thanh Le Huynh[2,3] and Hoang Thai Nguyen[2,3]

Abstract

Non-platinum electrodes for photoelectric devices are challenging and attractive to the scientific community. A thin film of molybdenum disulfide (MoS_2) was prepared on substrates coated with fluorine-doped tin oxide (FTO) to substitute the platinum counter electrode (CE) for dye-sensitized solar cells (DSSCs). Herein, we synthesized layered and honeycomb-like MoS_2 thin films via the cyclic voltammetry (CV) route. Thickness and morphology of the MoS_2 thin films were controlled via the concentration of precursor solution. The obtained results showed that MoS_2 thin films formed at a low precursor concentration had a layered morphology while a honeycomb-like MoS_2 thin film was formed at a high precursor concentration. Both types of MoS_2 thin film were composed of 1T and 2H structures and exhibited excellent electrocatalytic activity for the I_3^-/I^- redox couple. DSSCs assembled using these MoS_2 CEs showed a maximal power conversion efficiency of 7.33%. The short-circuit value reached 16.3 $mA·cm^{-2}$, which was higher than that of a conventional Pt/FTO CE (15.3 $mA·cm^{-2}$). This work reports for the first time the possibility to obtain a honeycomb-like MoS_2 thin film morphology by the CV method and investigates the effect of film structure on the electrocatalytic activity and photovoltaic performance of CEs for DSSC application.

Introduction

Since Grätzel's first report in 1991, dye-sensitized solar cells (DSSCs) have been the subject of much research due to the easy fabrication process and respectable efficiency [1]. This promising third generation of solar cells contains a dye-adsorbed TiO_2 photoanode, an iodide/triiodide electrolyte, and a platinum-based cathode, also known as the counter electrode (CE). How-

ever, the high cost of platinum has prevented the real-world application of DSSCs, which has led researchers to explore efficient cathode materials for DSSCs beyond platinum. To date, Pt replacement materials are divided into three categories, namely carbonaceous materials [2-5], conductive polymers [5], and transition metal compounds [6-8]. Transition metal compounds are considered a potential approach due to the high activity and acceptable price. Molybdenum disulfide (MoS_2) has recently gained a lot of attention due to its layered structure, cost efficiency, and superior catalytic activity [9-16]. MoS_2 exhibits layered structures with three types of crystal phase, that is, trigonal (1T), hexagonal (2H), and rhombohedral (3R). Considering electrocatalytic applications, the 1T metallic phase exhibits a higher catalytic activity than the 2H and 3R semiconductor phases [11,17]. Moreover, it is well known that the electrocatalytic activity of MoS_2 strongly depends on the number of catalytically active sites located at the edge planes [1,18,19]. These unsaturated Mo and S edges of MoS_2 enable the generation of the I_3^-/I^- redox couple, making it a potential CE for DSSCs. So far, MoS_2-based CEs for DSSCs have been fabricated and investigated using various techniques such as chemical bath deposition [1], sputtering [2], hydrothermal synthesis [10-13], wet chemistry [14], thermal reduction [15], and electrodeposition (ED) [20]. Among these methods, ED shows many advances thanks to its simplicity and rapidity. Additionally, it allows for the direct deposition of MoS_2 thin films from liquid precursors onto various conducting substrates with easily controlled thickness and morphology.

Several reports have already been published that describe the control of structure and morphology of electrodeposited MoS_2 to maximize its catalytic activity. Li et al. reported the synthesis of MoS_2/graphene composite films on FTO, which were directly used as CE for DSSCs without further thermal treatment. The power conversion efficiency (PCE) of the DSSCs was 8.01%, which was comparable to that of a Pt CE (8.21%) [21]. Quy et al. prepared MoS_2/FTO. The resulting DSSCs showed a PCE of 7.16%, similar to that of a Pt/FTO CE (7.48%). The MoS_2 film was amorphous and contained agglomerated clusters of nanoparticles [22]. Recently, Gurulakshmi et al. reported on DSSCs using a flexible CE fabricated by electrodeposition of a MoS_2 thin film onto a conductive FTO/PET substrate. The PCE of this flexible DSSCs reached 4.84%. The MoS_2 film was composed of sheets with a length of about 6 μm and a thickness of about 500 nm [23]. Another report by Chang et al. mentioned the change in morphology of MoS_2 from sphere-like shapes with large grain size to a uniform thin layer when changing the ED technique from potentiostatic (PS) mode to potential-reversal (PR) mode. This resulted in an improvement in PCE from 6.89% to 8.77% [24]. In general, above studies still have limits such as depositing MoS_2 on graphene or
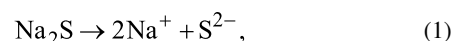
carbon dots, instead of directly developing the FTO substrate. In addition, the effect of thickness and morphology of MoS_2/FTO on the performance of DSSCs was not examined in these studies.
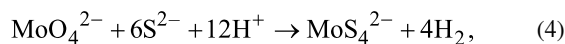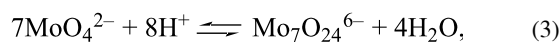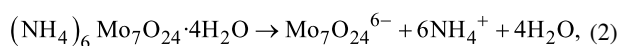
In this work, thin films of MoS_2 with two different shapes (layered and honeycomb-like) were deposited on FTO substrates from an aqueous precursor solution containing $(NH_4)_6Mo_7O_{24}\cdot4H_2O$ and Na_2S by cyclic voltammetry (CV). Morphology and thickness of the MoS_2 thin films were controlled by adjusting the concentration of the precursor solution. The electrochemical catalytic activity of the MoS_2 thin films was investigated regarding the I_3^-/I^- redox couple. The as-prepared MoS_2 thin films were directly used as CE for DSSCs. The structure and morphology of the MoS_2 thin films and their corresponding DSSC performance have been carefully evaluated. Furthermore, the effect of MoS_2 film thickness on the performance of DSSCs has also been discussed. It should be noted that this is the first report dealing with the fabrication of MoS_2 honeycomb-like thin films for DSSC application.

Results and Discussion
Electrodeposition of MoS_2 thin films

Electrodeposition of MoS_2 thin films was carried out from precursor solutions containing a mixture of $(NH_4)_6Mo_7O_{24}$ and Na_2S in KCl electrolyte solution. To study the redox behavior of the solution, the CV curves for each component and the mixture solutions were recorded in the potential range from −1.5 V to 1.0 V (Figure 1). The blank KCl electrolyte exhibits a straight line around zero current, while the precursor solutions show redox peaks associated with the oxidation/reduction of the precursor ions on the surface of the FTO electrode. In detail, the CV recorded in Na_2S solution shows a broad anodic peak around −0.50 V due to the oxidation of S^{2-} ions [25,26]. The CV curve of $(NH_4)_6Mo_7O_{24}$ solution exhibited two redox couple peaks at −0.34 V/−0.76 V and −0.77 V/−1.34 V attributed to the redox reactions of $Mo_7O_{24}^{6-}$ and MoO_4^{2-} ions, respectively [27]. The presence of MoO_4^{2-} ions is due to the equilibrium in Equation 3, which occurs in acidic solution of $(NH_4)_6Mo_7O_{24}$ (the pH here is about 4.3). The CV recorded in the mixture solution showed two oxidation peaks at −0.20 V and −0.50 V attributed to the oxidation of $Mo_7O_{24}^{6-}$ and S^{2-} ions, respectively. Moreover, a new reduction peak appeared around −1.20 V related to the reduction of MoS_4^{2-} to form MoS_2 as described in Equation 5. This CV behavior is similar to that of $(NH_4)_2MoS_4$ reported by Falola and co-workers [28]. The formation of MoS_4^{2-} ions in the mixture solution is detailed in Equations 1–4 [27-30]:

$$Na_2S \rightarrow 2Na^+ + S^{2-}, \qquad (1)$$

$$\left(NH_4\right)_6 Mo_7O_{24}\cdot 4H_2O \rightarrow Mo_7O_{24}^{\,6-} + 6NH_4^{\,+} + 4H_2O, \quad (2)$$

$$7MoO_4^{\,2-} + 8H^+ \rightleftharpoons Mo_7O_{24}^{\,6-} + 4H_2O, \quad (3)$$

$$MoO_4^{\,2-} + 6S^{2-} + 12H^+ \rightarrow MoS_4^{\,2-} + 4H_2, \quad (4)$$

$$MoS_4^{\,2-} + 6H^+ + 2e^- \rightarrow MoS_2 + 2H_2S + H_2. \quad (5)$$

It should be noted that $(NH_4)_2MoS_4$ is poorly soluble in water. Hence, the in situ synthesis of $MoS_4^{\,2-}$ from $(NH_4)_6Mo_7O_{24}$ (high solubility) and Na_2S in acidic media (adjusted to pH 6) is very favorable to the preparation of $MoS_4^{\,2-}$ precursor solution. In this work, the optimal concentration ratio of $(NH_4)_2Mo_7O_{24}$ (mM) to Na_2S (g/L) was found to be 1:6 (data not shown).

It can be seen from the CV curve of the mixture solution that the reduction of $MoS_4^{\,2-}$ occurred beginning at a potential of −0.80 V. Electrodeposition of MoS_2 at high overpotential leads to the formation of thick films [28]. To obtain thin films, we limited the deposition potential range of MoS_2 to a range between −1.0 V and 1.0 V and studied the effect of the concentration of the precursor solution on the morphology and the electrocatalytic activity of the MoS_2 thin films. The CVs (10 cycles) for the MoS_2 electrodeposition from solution 2.5 (see Experimental section for the denomination of the sample solutions) are shown in Figure 2a. The comparison of the tenth cycle of the CV recorded in different concentrations of precursor solution (solution 1.25, 2.5, and 5.0) is shown in Figure 2b. The presence of the redox couple peak at −0.2/−0.75 V can be attributed to the redox reactions of $Mo_7O_{24}^{\,6-}$ ions (the anodic peak is slightly shifted towards the anodic potential compared to that of
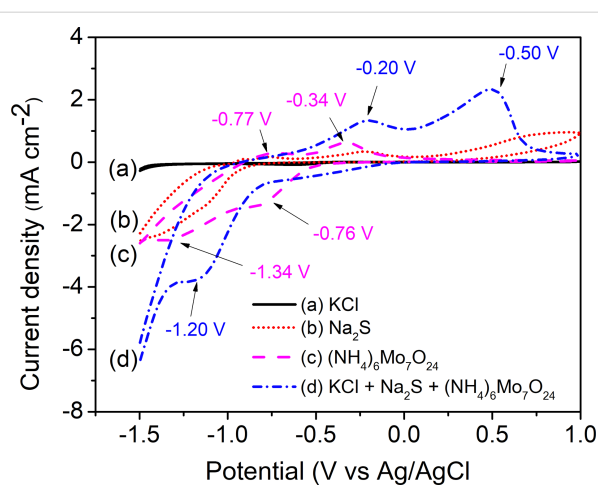

Figure 1: CV curves recorded in the solutions of (a) 0.1 M KCl, (b) 30 g/L Na_2S, (c) 5 mM $(NH_4)_6Mo_7O_{24}$, and (d) a mixture of 30 g/L Na_2S and 5 mM $(NH_4)_6Mo_7O_{24}$ in 0.1 M KCl, pH 6, using an FTO electrode, at scan rate of 100 mV·s^{-1}.

the $(NH_4)_2Mo_7O_{24}$ solution, see the insert in Figure 2a). The current density of the CV curves increases with the increase of precursor solution concentration. This allows one to predict that the thickness of MoS_2 film will be increased in the order: solution 1.25 < solution 2.5 < solution 5.0.

Morphology and structure of MoS$_2$ thin films

Morphology and thickness of MoS_2 films prepared on the FTO substrate were analyzed by FE-SEM. The MoS_2 films formed from solutions 1.25 and 2.5 exhibited thin-layered structures, which exposed edge sites (Figure 3a–c). The same structure had been found in the reports of Falola and Lin [24,28]. However, the film thickness of MoS_2 in these reports was thick compared to our results. Interestingly, the formation of MoS_2 film from solution 5.0 showed a homogenous honeycomb-like structure
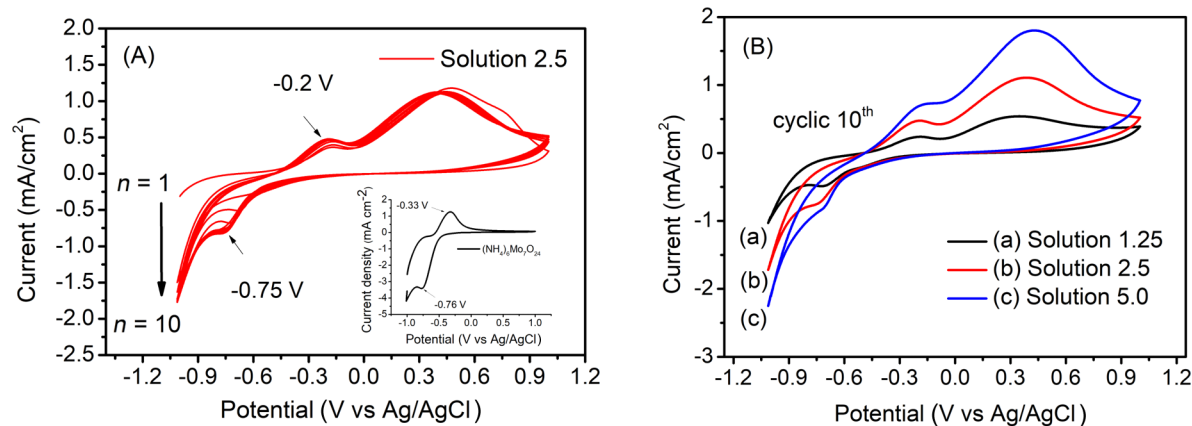

Figure 2: (a) CVs recorded during electrodeposition of MoS_2 from solution 1.25; (b) comparison of the tenth cycle of CVs recorded in solutions 1.25, 2.5, and 5.0; a scan rate of 100 mV·s^{-1} was used.

(Figure 3e). The surface of the film consists of honeycomb grids with a diameter of around 50 nm (see Figure 3e, insert). The roughness of the films was further studied by AFM. The film with the honeycomb-like structure showed the highest average roughness (S_a) and root mean square roughness (S_q) of 24.179 and 30.443 nm, respectively (see Supporting Information File 1, Figure S1 and Table S1). To the best of our knowledge, this is the first report on this type of MoS_2 film synthesized by CV. The potential range of the CV and the concentration of the precursor solution strongly affect the thickness and morphology of the MoS_2 films. The thickness of MoS_2 films was estimated from cross-sectional FE-SEM images. The for-

mation of MoS_2 from solutions 2.5 and 5.0 yielded thicknesses of about 50 nm and 500 nm, respectively (Figure 3d,f).

The phase structure of the electrodeposited MoS_2 thin films was identified by XRD and Raman analyses. The XRD pattern and the Raman spectrum of the MoS_2 thin film deposited from solution 5.0 are presented in Figure 4. The XRD pattern of the MoS_2/FTO samples shows only the peaks of the FTO substrate because the MoS_2 thin film is amorphous or too thin (Figure 4a) [22-24]. Thus, the electrodeposited thin film was further characterized by Raman spectroscopy. The Raman spectrum of the MoS_2/FTO sample showed the characteristic peaks of the 2H
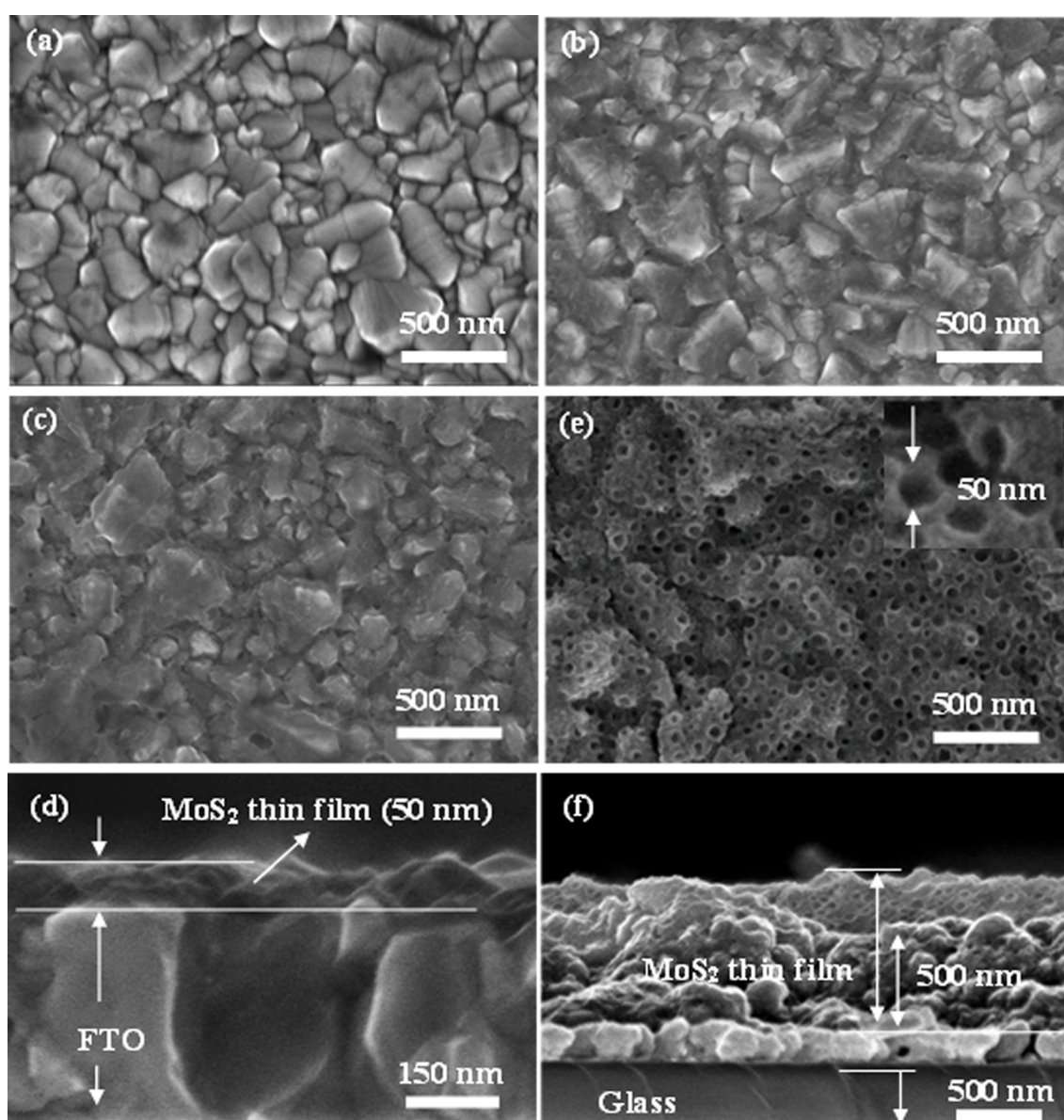

Figure 3: FE-SEM images (top view and cross-sectional view) of (a) FTO and (b–f) MoS_2 deposited on FTO from different precursor solution concentrations: (b) solution 1.25, (c ,d) solution 2.5, and (e, f) solution 5.0.
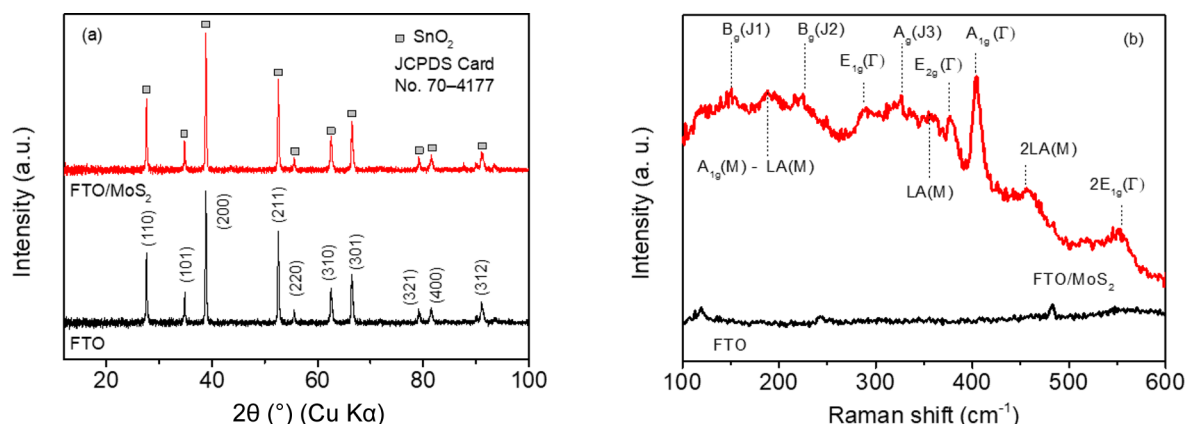
Figure 4: (a) XRD patterns and (b) Raman spectra of the FTO substrate and a thin film of MoS$_2$ electrodeposited from solution 5.0.

and 1T phases of MoS$_2$ (Figure 4b). The appearance of the J$_1$, J$_2$, and J$_3$ peaks around 150, 226, and 326 cm^{-1} confirmed the presence of the 1T metallic phase. Whereas the two Raman vibration modes, E$_{2g}$ (in plane) and A$_{1g}$ (out of plane), observed at 376 and 403 cm^{-1}, respectively, are attributed to the 2H semiconductor phase [31-33]. The three first-order Raman modes, A$_{1g}$, E$_{2g}$, and E$_{1g}$ (288 cm^{-1}), are attributed to vibrational modes of the S–Mo–S layer. Other well-known multiphonon bands, namely A$_{1g}$-LA (188 cm^{-1}), LA (355 cm^{-1}), 2LA (455 cm^{-1}), and 2E$_{1g}$ (553 cm^{-1}) have also been observed [34-36]. The 1T phase exhibits a higher electroactivity than the 2H phase. Also, the 1T phase tends to transform into the 2H phase at high temperatures (Figure 4b) [1,17,36]. Therefore, the freshly prepared MoS$_2$/FTO electrodes (without heat treatment) were used to examine the electrocatalytic activity towards the I$_3^-$/I$^-$ redox couple as well as directly used as CEs for DSSCs.

Electroactivity of MoS$_2$ CEs

The electrocatalytic activity of MoS$_2$ CEs towards the I$_3^-$/I$^-$ redox couple was investigated and compared to that of a Pt CE. As can be seen in Figure 5, there are two redox pairs (Ox$_1$/Red$_1$) and (Ox$_2$/Red$_2$). These redox peaks were well defined as the oxidation and reduction of iodide and triiodide (3I$^-$ − 2e$^-$ → I$_3^-$ (Ox$_1$), I$_3^-$ + 2e$^-$ → 3I$^-$ (Red$_1$) and 2I$_3^-$ − 2e$^-$ → 3I$_2$ (Ox$_2$), 3I$_2$ + 2e$^-$ → 2I$_3^-$ (Red$_2$) [6-9].

Since the reduction of I$_3^-$ to I$^-$ on the CE plays a vital role in the regeneration of the oxidized dye molecules on the photoanode of the DSSCs, the electrocatalytic behavior of MoS$_2$ CEs was further evaluated regarding the first redox couple (Ox$_1$/Red$_1$). Various parameters including anode/cathode peak potentials (E_{pOx1}, E_{pRed1}), peak-to-peak voltage separation (E_{pp}), and anode/cathode peak current densities (J_{Ox1}, J$_{Red1}$) were calculated and presented in Table 1. The E_{pp} value for MoS$_2$ CEs was slightly larger than that of Pt CE
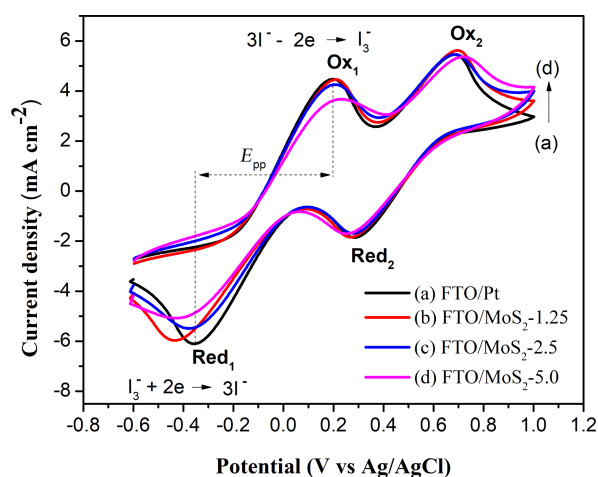

Figure 5: CV curves of MoS$_2$ CEs prepared with different concentrations of reaction precursors compared to that of Pt CE, recorded in ACN solution of 10 mM I$_2$, 20 mM KI, and 0.1 M LiClO$_4$; a scan rate of 100 mV·s^{-1} was used.

confirming their excellent electrocatalytic activity. The J_{Red1} values of MoS$_2$ CEs decreased in the order: MoS$_2$-1.25 ≈ Pt > MoS$_2$-2.5 > MoS$_2$-5.0 (see Table 1). This demonstrated that increasing the concentration of the precursor solution resulted in the increase in the thickness of the MoS$_2$ film and, thus, reduced the electrocatalytic activity.

Further study of the electrocatalytic behavior of the MoS$_2$ CEs was carried out by using the EIS technique under dark conditions using full cells assembled from different MoS$_2$/FTO CEs or a Pt/FTO CE. The Nyquist plots for these cells exhibited two semicircles as presented in Figure 6. The first semicircle in the high-frequency region is associated with the reduction of I$_3^-$ at the cathode (CE/electrolyte), while the second one in the low-frequency region is attributed to electron transport in the TiO$_2$

Table 1: Electrochemical parameters from CV measurements of MoS$_2$ and Pt CEs.

CE	E_{pOx1} (V)	E_{pRed1} (V)	E_{pp} (V)	J_{Ox1} (mA·cm^{-2})	J_{Red1} (mA·cm^{-2})
Pt	0.195	−0.355	0.550	4.450	−6.059
MoS$_2$-1.25	0.208	−0.432	0.640	4.476	−5.965
MoS$_2$-2.5	0.208	−0.373	0.581	4.257	−5.511
MoS$_2$-5.0	0.226	−0.415	0.641	3.695	−5.057

film in the back reaction at the TiO$_2$/electrolyte interface (TiO$_2$/dye/electrolyte). EIS data were fitted using an equivalent-circuit model including the series resistances of electrolyte and FTO substrate (R_s) and the charge-transfer resistances on the CE/electrolyte and TiO$_2$/dye/electrolyte interfaces (R_{ct1} and R_{ct2}) associated with the corresponding constant phase elements (CPE1 and CPE2) as described in Figure 6 (Figure 6, insert).
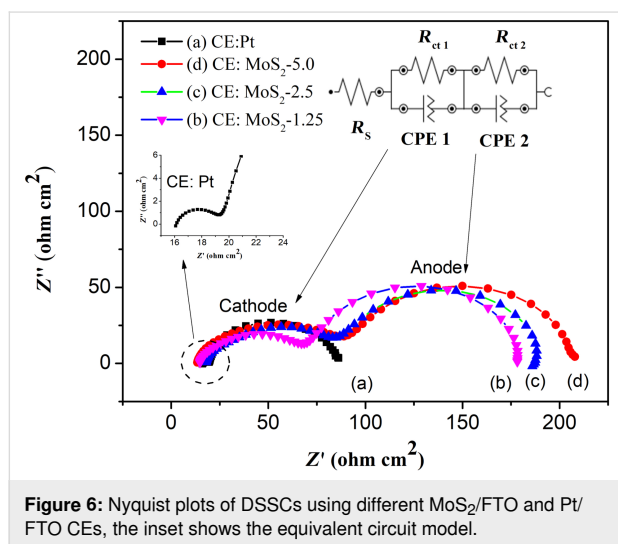
Figure 6: Nyquist plots of DSSCs using different MoS$_2$/FTO and Pt/FTO CEs, the inset shows the equivalent circuit model.

The fit values for R_s and R_{ct1} reflect the catalytic behavior of CEs in DSSCs and are presented in Table 2. The R_s value for MoS$_2$ CE-based DSSCs slightly increased with the thickness of the films and is comparable to that of Pt CE-based DSSCs. This is due to the high conductivity of the metallic 1T phase of MoS$_2$

and is in good agreement with Raman analysis. Under dark conditions, the R_{ct1} value for MoS$_2$ CE-based DSSCs (from 52.6 to 78.5 Ω·cm^2) was found to be significantly higher than that of Pt CE-based DSSCs (3.6 Ω·cm^2), indicating slower charge transfer kinetics at the MoS$_2$/electrolyte interface compared to the Pt/electrolyte interface. The high peak current density value for I$_3^-$ reduction from CV analysis obtained for MoS$_2$-based CEs was therefore attributed to the high number of catalytically active sites located on the edge planes of the MoS$_2$ films.

DSSC performance
To further evaluate the effect of MoS$_2$ morphology and thickness on the performance of the DSSCs, the photovoltaic performance of DSSCs using different MoS$_2$ CEs was investigated under illumination. The *J–V* curves and the corresponding photovoltaic parameters of DSSCs are given in Figure 7 and Table 2, respectively. The DSSC using MoS$_2$-1.25/FTO CE displayed an excellent photovoltaic performance compared to that with a Pt/FTO a CE. In particular, the obtained value of 16.3 mA·cm^{-2} for the short-circuit photocurrent (J_{sc}) was found to be higher than that of Pt/FTO CE (15.3 mA·cm^{-2}). This is attributed to the high number of catalytically active sites together with the low resistance of this MoS$_2$ film.

Although the electrocatalytic ability regarding the reduction of I$_3^-$ of MoS$_2$ was lower than that of Pt, other parameters including an open-circuit voltage (V_{oc}) of 0.69 V, a fill factor (FF) of 0.66, and a PCE of 7.33% of this MoS$_2$ CE-based DSSCs were comparable to those of a DSSC based on a Pt CE (V_{OC} = 0.75 V, FF = 0.75, PEC = 8.66%) and to values found in

Table 2: Photovoltaic parameters and EIS data of the DSSCs based on different MoS$_2$ CEs and a Pt CE.

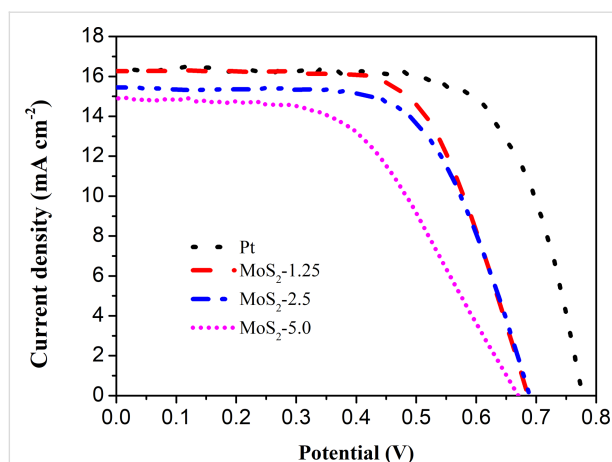| CE	J_{sc} (mA·cm^{-2})	V_{oc} (V)	FF	η (%)	R_s (Ω·cm^2)	R_{ct1} (Ω·cm^2)	τ (ms)
Pt	15.30	0.75	0.75	8.66	16.1	3.60	23
MoS$_2$-1.25	16.30	0.69	0.66	7.33	14.8	52.6	30
MoS$_2$-2.5	14.85	0.68	0.63	6.39	16.6	65.8	31
MoS$_2$-5.0	14.90	0.67	0.53	5.31	17.5	78.5	40

Figure 7: Photovoltaic performance of DSSCs fabricated with different MoS$_2$/FTO and Pt/FTO CEs.

other reports (Table 3). The PCE for DSSCs using MoS$_2$ with different thicknesses decreased in the order: MoS$_2$-1.25 (very thin film) > MoS$_2$-2.5 (50 nm) > MoS$_2$-5.0 (500 nm). This is in good agreement with the trend of R_s and R_{ct1} values (see Table 2 and Table 3). The effect of film thickness on the electrical conductivity of the MoS$_2$ films was also investigated by *I–V* measurements (see Supporting Information File 1, Figure S2 and Table S1). The electrical conductivity of the as-pre-

pared MoS$_2$ decreased in the order: MoS$_2$-1.25 (75 mS·cm^{-1}) > MoS$_2$-2.5 (61 mS·cm^{-1}) > MoS$_2$-5.0 (46 mS·cm^{-1}). This suggests that the thickness of the MoS$_2$ film has a significant effect on the catalytic ability and photovoltaic performance of the CE in DSSCs. Additionally, the electron lifetime (τ) indicates the recombination kinetics of electrons in the mesoscopic TiO$_2$ film of the DSSCs. This parameter can be calculated from the peak frequency (f_{max}) of the low-frequency semicircles ($\tau = 1/2\pi f_{max}$). The τ values measured under dark conditions for DSSCs devices fabricated from various CEs are presented in Table 2. The τ values for DSSCs fabricated with MoS$_2$ CEs were higher than those of a DSSC using a Pt CE and increased in the order: DSSCs-MoS$_2$-1.25 < DSSCs-MoS$_2$-2.5 < DSSCs-MoS$_2$-5.0. A longer electron lifetime indicates a slower recombination process within the DSSCs fabricated with MoS$_2$/FTO CEs. The stability of the devices was tested by repeating the *I–V* measurements every week (Supporting Information File 1, Figure S3). The PCE value of a DSSC fabricated using MoS$_2$-1.25 showed a slight decrease of 2.6% and reached stability after two weeks of testing under ambient conditions. This suggested that the MoS$_2$-1.25/FTO CE has reversible redox activity and electrochemical stability. The electrochemical stability of the MoS$_2$/FTO CE should provide long-term stability for solar cell devices. However, more work needs to be done to improve the efficiency of this DSSC device [36-39].

Table 3: Performance summary of MoS$_2$-based CEs for DSSCs.

MoS$_2$ CE	Method	V_{oc} (V)	J_{sc} (mA·cm^{-2})	FF	η (%)	Ref
MoS$_2$/FTO	chemical bath deposition	0.73	15.92	0.61	7.14	[1]
MoS$_2$/FTO	sputtering	0.71	13.17	0.64	6.00	[9]
MoS$_2$/FTO	hydrothermal	0.70	18.37	0.58	7.41	[10]
1T MoS$_2$/FTO	hydrothermal	0.73	18.76	0.52	7.08	[11]
2H MoS$_2$/FTO	hydrothermal	0.73	6.78	0.35	1.72	[11]
MoS$_2$/FTO	hydrothermal	0.74	16.96	0.66	8.28	[12]
porous MoS$_2$/FTO	hydrothermal/spin coating	0.76	15.4	0.53	6.35	[13]
flower-shaped MoS$_2$/FTO	hydrothermal/spin coating	0.70	13.73	0.52	5.23	[13]
MoS$_2$/FTO	wet-chemical process	0.68	18.46	0.58	7.01	[14]
MoS$_2$/FTO	spin coating/thermal reduction	0.73	16.91	0.52	6.35	[15]
multilayered MoS$_2$/FTO	spray coating	0.75	15.81	0.25	2.92	[16]
few-layered MoS$_2$/FTO	exfoliation of ML-MoS$_2$ powder and spray coating technique	0.74	14.90	0.16	1.74	[16]
MoS$_2$ nanoparticles/FTO	thermal decomposition	0.75	14.72	0.49	5.41	[16]
MoS$_2$/FTO	potentiostatic	0.72	15.68	0.63	7.16	[22]
MoS$_2$/FTO	potentiostatic	0.78	16.18	0.54	6.89	[24]
MoS$_2$/FTO	potential reversal	0.76	16.16	0.71	8.77	[24]
layered MoS$_2$/FTO	cyclic voltammetry	0.69	16.29	0.66	7.33	this work
honeycomb-like MoS$_2$/FTO	cyclic voltammetry	0.67	14.90	0.53	5.31	this work

Conclusion

We synthesized successfully MoS_2 thin films with layered or honeycomb-like structures onto FTO substrates by the CV route. The morphology and thickness of the MoS_2 films can be effectively controlled by adjusting the concentration of the precursor solution. In detail, MoS_2 formed a layered thin film with a thickness of about 50 nm when the concentration level ratio between $(NH_4)_2Mo_7O_{24}$ and Na_2S was 2.5/15 (solution 2.5, see Experimental section). Honeycomb MoS_2 was formed with a thickness of about 500 nm from solution 5.0 (with a concentration level ratio between $(NH_4)_2Mo_7O_{24}$ and Na_2S of 5/30). In addition, as-prepared MoS_2 films have been used as an alternative CE to Pt in DSSCs. The short-circuit photocurrent (J_{sc}) was higher than that of a Pt/FTO CE. Moreover, the highest performance of solar cells was found with the layered MoS_2 film thank to good electrical conductivity, a high number of catalytically active sites, and the thickness of the MoS_2 film. The MoS_2/FTO films could be applied as non-Pt electrodes for DSSCs in the near future.

Experimental
Materials and reagents

Ammonium molybdate tetrahydrate ($(NH_4)_6Mo_7O_{24}\cdot4H_2O$, 99.98%), sodium sulfide nonahydrate ($Na_2S\cdot9H_2O$, 99.99%), potassium chloride (KCl, 99%), acetonitrile (ACN, CH_3CN, 99%), dimethyl sulfoxide (DMSO, $(CH_3)_2SO$, 99.5%), ethanol (EtOH, CH_3CH_2OH, 99.8%), guanidinium thiocyanate ($NH_2C(=NH)NH_2\cdot HSCN$, 99%), iodine (I_2, 99.8%), 1-methyl-3-propylimidazolium iodide ($C_7H_{13}IN_2$, 98%), 4-*tert*-butylpyridine ($C_9H_{13}N$, 98%), valeronitrile ($CH_3(CH_2)_3CN$, 99.5%), chloroplatinic acid hexahydrate ($H_2PtCl_6\cdot6H_2O$, ≥37.50% Pt), sulfuric acid (H_2SO_4, 95–98%), polyvinylpyrrolidone (PVP, $(C_6H_9NO)_n$, average M_w 10,000), and sodium borohydride ($NaBH_4$, 99%) were purchased from Sigma-Aldrich (Germany). Low-temperature thermoplastic sealant (Surlyn, 25 μm), 18NR-T transparent titania paste (particle size of 20 nm), 18NR-AO active opaque titania paste (particle sizes of 20 and 450 nm), fluorine-doped tin oxide (FTO, TEC8 glass plates, 8 $\Omega\cdot cm^{-2}$, 2.2 mm thickness), and N719 industry standard dye (N719) were purchased from Dyesol (Australia). All commercial chemicals were of analytical grade and were used as supplied without further purification.

Electrodeposition of MoS_2 thin films

Thin films of MoS_2 with different morphologies were electrodeposited onto FTO substrates by the CV method. MoS_2 electrodeposition was carried out using an Autolab 302 N (Eco chemie, Netherlands) connected to a three-electrode cell. Accordingly, a Pt mesh, an Ag/AgCl (ALS, Japan), and the FTO plate (1.5 × 1.5 cm) were used as the counter electrode (CE), the reference electrode (RE), and the working electrode (WE),

respectively. Prior to CV electrodeposition, the FTO substrates were first cleaned in a 1% Hellmanex solution at 70 °C for 30 min in an ultrasonic bath, then washed three times in distilled water, dried by nitrogen flow, and finally treated in a UV ozone chamber for 5 min to obtain the cleaned FTO electrode. Precursor solutions were prepared by dissolving $(NH_4)_6Mo_7O_{24}$ (*x* mM) and Na_2S (*y* $g\cdot L^{-1}$) in distilled water, the pH of the solution was adjusted to 6.0 using a 20% (v/v) H_2SO_4 solution, KCl (0.1 M) was used as the supporting electrolyte. The concentration ratio between $(NH_4)_2Mo_7O_{24}$ and Na_2S was kept constant (*x*/*y* = 1:6) with different concentration levels including 1.25:7.5 (solution 1.25), 2.5:15 (solution 2.5), and 5:30 (solution 5.0). The CV measurement was performed under a dynamic potential between −1.0 V and 1.0 V for ten cycles at a scan rate of 100 $mV\cdot s^{-1}$ in a nitrogen atmosphere.

Fabrication of DSSCs

DSSCs with an active area of 0.25 cm^2 were assembled using the pre-cleaned FTO plates (1.5 × 1.5 cm) for the fabrication of anode and cathode. For cathode preparation, MoS_2/FTO CEs were prepared with different morphologies from the above MoS_2 samples. The obtained CEs were designated as MoS_2-1.25/FTO, MoS_2-2.5/FTO, and MoS_2-5.0/FTO. For comparison, a Pt-based CE (Pt/FTO) was fabricated by soaking the cleaned FTO glasses in PVP–platinum suspension at 45 °C for 5 min, followed by washing with distilled water. The PVP–platinum suspension was prepared as follows: First, 1.0 g of H_2PtCl_6 was dissolved in 150 mL of distilled water, then 0.5 g PVP was added to the above solution under stirring for 10 min. Finally, to this solution, $NaBH_4$ solution (1.17 g $NaBH_4$ was dissolved in 124.8 mL of distilled water, stirred for 3 min) was added at a rate of 1.5 mL/min until the color of the mixture solution turned into black.

For the fabrication of the photoanodes, the cleaned FTO electrodes were first pretreated by immersion in a 40 mM $TiCl_4$ solution at 70 °C for 30 min and rinsed with distilled water and ethanol. The treated FTO electrodes were then successively coated with a transparent 18NR-T titania paste (three layers) and an active opaque 18NR-AO titania paste (one outer layer) by the screen-printing method using 43T mesh. The printed electrodes were dried at room temperature for 5 min, then at 120 °C for 5 min after each printed layer, and finally heated at 450 °C under airflow for 30 min. When the temperature was cooled down to 70 °C, the electrodes were dipped in N719 dye (0.3 M N719 in the mixture DMSO/EtOH, v/v = 1:9) for 12 h to obtain the photoanodes.

For cell assembly, the DSSCs were fabricated in a nitrogen atmosphere using a glove box. Typically, the photoanode and the MoS_2-based CE were sealed together by a hot-melt Surlyn film

using a thermopress, pressed at 170 °C for 15 s. The electrolyte solution (0.1 M guanidinium thiocyanate, 0.03 M iodine, 1 M 1-methyl-3-propylimidazolium iodide, 0.5 M 4-*tert*-butylpyridine in a mixture of valeronitrile/acetonitrile with a volume ratio of 0.15:0.85) was then injected into the cell through predrilled holes on the CE. The holes were then covered with a thin glass slide using the same thermopress method as described above to obtain DSSC devices. DSSCs assembled using the CE fabricated from precursor solutions 1.25, 2.5, and 5.0 were denoted as DSSCs-MoS$_2$-1.25, DSSCs- MoS$_2$-2.5, and DSSCs-MoS$_2$-5.0, respectively. For comparison, DSSCs based on Pt/FTO CE (DSSCs-Pt) were also fabricated under the same conditions.

Characterizations of MoS$_2$ thin films

X-ray diffraction (XRD) analysis was carried out using a D8 Advance (Bruker, Germany) with a copper anode ($\lambda_{K\alpha}$ = 1.54 Å). Raman spectroscopy measurements were performed on a LabRAM HR 800 Raman Spectrometer (HORIBA Jobin Yvon) with an excitation laser source at 532 nm. The morphology of MoS$_2$ thin films was analyzed by an ultrahigh-resolution field-emission scanning electron microscope (FE-SEM, Hitachi SU-8010, Japan). The electrochemical catalytic activity of the MoS$_2$-based CEs was studied regarding the I$_3^-$/I$^-$ redox couple (prepared with 10 mM I$_2$, 20 mM KI, and 0.1 M LiClO$_4$ in acetonitrile) and compared to that of a FTO/Pt CE by CV.

DSSC characterizations

Photoelectrochemical measurements were performed using an Oriel Sol1A class ABB solar simulator (Oriel-Newport-USA, Model No. 94061A). Simulated sunlight of 100 mW·cm^{-2} (1 sun) was generated and corrected by a 1000 W Xe lamp and an AM 1.5 filter. The photocurrent density–voltage (*J–V*) curves of the DSSCs were measured using a Keithley model 2400 multisource meter. Electrochemical impedance spectroscopy (EIS) of the fabricated DSSCs was carried out using an Autolab 302 N equipped with a FRA 32M module. The EIS measurements were carried out at open-circuit voltage with an alternating voltage amplitude of 10 mV under dark conditions in a frequency range between 0.01 Hz and 100 kHz. The efficiency of the DSSCs was analyzed and reported as the average of three cells.

Supporting Information

Supporting Information File 1

Additional experimental data.
[https://www.beilstein-journals.org/bjnano/content/supplementary/2190-4286-13-44-S1.pdf]

ORCID® iDs

Hai Viet Le - https://orcid.org/0000-0001-7480-806X

References

1. Vikraman, D.; Patil, S. A.; Hussain, S.; Mengal, N.; Kim, H.-S.; Jeong, S. H.; Jung, J.; Kim, H.-S.; Park, H. J. *Dyes Pigm.* **2018,** *151,* 7–14. doi:10.1016/j.dyepig.2017.12.037
2. Roy-Mayhew, J. D.; Bozym, D. J.; Punckt, C.; Aksay, I. A. *ACS Nano* **2010,** *4,* 6203–6211. doi:10.1021/nn1016428
3. Chen, J.; Li, K.; Luo, Y.; Guo, X.; Li, D.; Deng, M.; Huang, S.; Meng, Q. *Carbon* **2009,** *47,* 2704–2708. doi:10.1016/j.carbon.2009.05.028
4. Yang, Z.; Chen, T.; He, R.; Guan, G.; Li, H.; Qiu, L.; Peng, H. *Adv. Mater. (Weinheim, Ger.)* **2011,** *23,* 5436–5439. doi:10.1002/adma.201103509
5. Lee, K. S.; Lee, H. K.; Wang, D. H.; Park, N. G.; Lee, J. Y.; Park, O. O.; Park, J. H. *Chem. Commun.* **2010,** *46,* 4505–4507. doi:10.1039/c0cc00432d
6. Li, C.-T.; Lee, C.-P.; Li, Y.-Y.; Yeh, M.-H.; Ho, K.-C. *J. Mater. Chem. A* **2013,** *1,* 14888–14896. doi:10.1039/c3ta12603j
7. Wu, M.; Wang, Y.; Lin, X.; Yu, N.; Wang, L.; Wang, L.; Hagfeldt, A.; Ma, T. *Phys. Chem. Chem. Phys.* **2011,** *13,* 19298–19301. doi:10.1039/c1cp22819f
8. Liu, C.-J.; Tai, S.-Y.; Chou, S.-W.; Yu, Y.-C.; Chang, K.-D.; Wang, S.; Chien, F. S.-S.; Lin, J.-Y.; Lin, T.-W. *J. Mater. Chem.* **2012,** *22,* 21057–21064. doi:10.1039/c2jm33679k
9. Hussain, S.; Shaikh, S. F.; Vikraman, D.; Mane, R. S.; Joo, O.-S.; Naushad, M.; Jung, J. *ChemPhysChem* **2015,** *16,* 3959–3965. doi:10.1002/cphc.201500644
10. Al-Mamun, M.; Zhang, H.; Liu, P.; Wang, Y.; Cao, J.; Zhao, H. *RSC Adv.* **2014,** *4,* 21277–21283. doi:10.1039/c4ra00583j
11. Wei, W.; Sun, K.; Hu, Y. H. *J. Mater. Chem. A* **2016,** *4,* 12398–12401. doi:10.1039/c6ta04743b
12. Liang, J.; Li, J.; Zhu, H.; Han, Y.; Wang, Y.; Wang, C.; Jin, Z.; Zhang, G.; Liu, J. *Nanoscale* **2016,** *8,* 16017–16025. doi:10.1039/c6nr03635j
13. Liu, W.; He, S.; Yang, T.; Feng, Y.; Qian, G.; Xu, J.; Miao, S. *Appl. Surf. Sci.* **2014,** *313,* 498–503. doi:10.1016/j.apsusc.2014.06.011
14. Patil, S. A.; Kalode, P. Y.; Mane, R. S.; Shinde, D. V.; Doyoung, A.; Keumnam, C.; Sung, M. M.; Ambade, S. B.; Han, S.-H. *Dalton Trans.* **2014,** *43,* 5256–5259. doi:10.1039/c3dt53356e
15. Lin, C.-H.; Tsai, C.-H.; Tseng, F.-G.; Yu, Y.-Y.; Wu, H.-C.; Hsieh, C.-K. *Nanoscale Res. Lett.* **2015,** *10,* 446. doi:10.1186/s11671-015-1156-0
16. Lei, B.; Li, G. R.; Gao, X. P. *J. Mater. Chem. A* **2014,** *2,* 3919–3925. doi:10.1039/c3ta14313a
17. Liu, Z.; Gao, Z.; Liu, Y.; Xia, M.; Wang, R.; Li, N. *ACS Appl. Mater. Interfaces* **2017,** *9,* 25291–25297. doi:10.1021/acsami.7b05775

18. Li, G.; Zhang, D.; Qiao, Q.; Yu, Y.; Peterson, D.; Zafar, A.; Kumar, R.; Curtarolo, S.; Hunte, F.; Shannon, S.; Zhu, Y.; Yang, W.; Cao, L. *J. Am. Chem. Soc.* **2016,** *138,* 16632–16638. doi:10.1021/jacs.6b05940

19. Jaramillo, T. F.; Jørgensen, K. P.; Bonde, J.; Nielsen, J. H.; Horch, S.; Chorkendorff, I. *Science* **2007,** *317,* 100–102. doi:10.1126/science.1141483

20. Aliyev, A. S.; Elrouby, M.; Cafarova, S. F. *Mater. Sci. Semicond. Process.* **2015,** *32,* 31–39. doi:10.1016/j.mssp.2015.01.006

21. Li, S.; Min, H.; Xu, F.; Tong, L.; Chen, J.; Zhu, C.; Sun, L. *RSC Adv.* **2016,** *6,* 34546–34552. doi:10.1039/c6ra02494g

22. Quy, V. H. V.; Vijayakumar, E.; Ho, P.; Park, J.-H.; Rajesh, J. A.; Kwon, J.; Chae, J.; Kim, J.-H.; Kang, S.-H.; Ahn, K.-S. *Electrochim. Acta* **2018,** *260,* 716–725. doi:10.1016/j.electacta.2017.12.023

23. Gurulakshmi, M.; Meenakshamma, A.; Siddeswaramma, G.; Susmitha, K.; Venkata Subbaiah, Y. P.; Narayana, T.; Raghavender, M. *Sol. Energy* **2020,** *199,* 447–452. doi:10.1016/j.solener.2020.02.047

24. Chang, C.-Y.; Anuratha, K. S.; Lin, Y.-H.; Xiao, Y.; Hasin, P.; Lin, J.-Y. *Sol. Energy* **2020,** *206,* 163–170. doi:10.1016/j.solener.2020.06.001

25. Ghayad, I. M.; Al Kharafi, F. M.; Saad, A. Y.; Ateya, B. G. *Mod. Appl. Sci.* **2010,** *4,* 2–11. doi:10.5539/mas.v4n3p2

26. Wang, L.; Lu, P.; Liu, C.; Wang, L. *Int. J. Electrochem. Sci.* **2015,** *10,* 8374–8384.

27. You, J.; Wu, D.; Liu, H. *Polyhedron* **1986,** *5,* 535–537. doi:10.1016/s0277-5387(00)84960-8

28. Falola, B. D.; Wiltowski, T.; Suni, I. I. *J. Electrochem. Soc.* **2016,** *163,* D568–D574. doi:10.1149/2.0011610jes

29. Ponomarev, E. A.; Neumann-Spallart, M.; Hodes, G.; Lévy-Clément, C. *Thin Solid Films* **1996,** *280,* 86–89. doi:10.1016/0040-6090(95)08204-2

30. Ghosh, S. K.; Bera, T.; Karacasu, O.; Swarnakar, A.; Buijnsters, J. G.; Celis, J. P. *Electrochim. Acta* **2011,** *56,* 2433–2442. doi:10.1016/j.electacta.2010.10.065

31. Tan, S. J. R.; Sarkar, S.; Zhao, X.; Luo, X.; Luo, Y. Z.; Poh, S. M.; Abdelwahab, I.; Zhou, W.; Venkatesan, T.; Chen, W.; Quek, S. Y.; Loh, K. P. *ACS Nano* **2018,** *12,* 5051–5058. doi:10.1021/acsnano.8b02649

32. Sharma, C. H.; Surendran, A. P.; Varghese, A.; Thalakulam, M. *Sci. Rep.* **2018,** *8,* 12463. doi:10.1038/s41598-018-30867-y

33. Nayak, A. P.; Pandey, T.; Voiry, D.; Liu, J.; Moran, S. T.; Sharma, A.; Tan, C.; Chen, C.-H.; Li, L.-J.; Chhowalla, M.; Lin, J.-F.; Singh, A. K.; Akinwande, D. *Nano Lett.* **2015,** *15,* 346–353. doi:10.1021/nl5036397

34. Windom, B. C.; Sawyer, W. G.; Hahn, D. W. *Tribol. Lett.* **2011,** *42,* 301–310. doi:10.1007/s11249-011-9774-x

35. Livneh, T.; Spanier, J. E. *2D Mater.* **2015,** *2,* 035003. doi:10.1088/2053-1583/2/3/035003

36. Blanco, É.; Afanasiev, P.; Berhault, G.; Uzio, D.; Loridant, S. *C. R. Chim.* **2016,** *19,* 1310–1314. doi:10.1016/j.crci.2015.08.014

37. Rashidi, S.; Rashidi, S.; Heydari, R. K.; Esmaeili, S.; Tran, N.; Thangi, D.; Wei, W. *Prog. Photovoltaics* **2021,** *29,* 238–261. doi:10.1002/pip.3350

38. Akman, E.; Akin, S.; Ozturk, T.; Gulveren, B.; Sonmezoglu, S. *Sol. Energy* **2020,** *202,* 227–237. doi:10.1016/j.solener.2020.03.108

39. Akman, E. *J. Mol. Liq.* **2020,** *317,* 114223. doi:10.1016/j.molliq.2020.114223